Vibration Analysis of Fluid Dynamic Bearing Spindles with Rotating-Shaft Design

Thitima Jintanawan, I. Y. Shen, and Katsuhiko Tanaka

***Abstract*—This paper is to present theoretical and experimental vibration analysis of fluid dynamic bearing (FDB) spindles with rotating-shaft design. In the theoretical analysis, a mathematical model is developed to predict half-speed whirls, rocking modes, frequency response functions, and shock responses. In the experimental studies, FDB spindles carrying multiple disks are tested at various spin speed. Frequency response functions (FRF) are obtained to verify the mathematical model. The theoretical results agree reasonably well with experimental results in both natural frequencies and resonance amplitudes.**

I. Introduction

FLUID dynamic bearing (FDB) spindles are being considered for HDD industry, because FDB spindles have significantly larger damping and lower acoustic noise. Currently, there are two types of spindle design: fixed-shaft design and rotating-shaft design. Fixed-shaft design, as shown in Fig. 1, consists of a rotating hub (rotor) carrying the disks, which is mounted on a stationary shaft (stator) through either ball bearings or FDB's. This design is widely used in ball-bearing spindles, and the mathematical model is available [1], [2]. Although this design has also been used for FDB spindles [3], it becomes difficult and expensive. A more desirable design is rotating-shaft design; see Fig. 2. The rotating shaft and hub (rotor) that carry the disks are pressed into the stationary bearing sleeve and the base plate (stator). This design has fewer components and the bearing lubricant is less likely to leak. Therefore, this design is becoming dominant among FDB spindles. This design, however, is more difficult to model, because the shaft is spinning, whirling, and rocking together with the hub and the disks. Because a mathematical model is not available, designers cannot accurately compare and evaluate the vibration performance of these two designs.

The purpose of this paper is to present theoretical and experimental vibration analysis of FDB spindle systems with rotating-shaft design. A mathematical model is developed to predict free and forced responses of the systems. Free vibration analysis of rotating-shaft spindles [4] shows that the hub deformation at the hub/shaft interface is critical in the rotating-shaft design, because a considerable load is transmitted. Modeling of the hub deformation can improve the prediction of rocking mode frequencies by 30% [4]. Further to these studies, this paper focuses on forced vibration analysis of FDB spindles with rotating-shaft design. Frequency response functions (FRF) are predicted and compared with experimental results to verify the mathematical model.

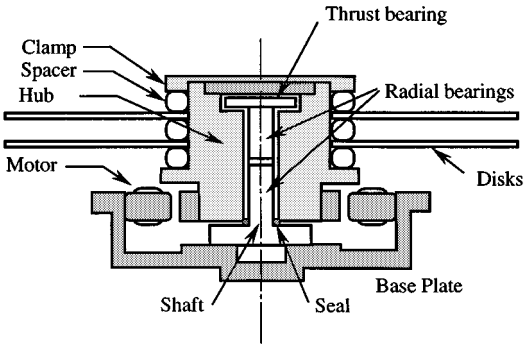

Fig. 1. A fixed-shaft spindle.

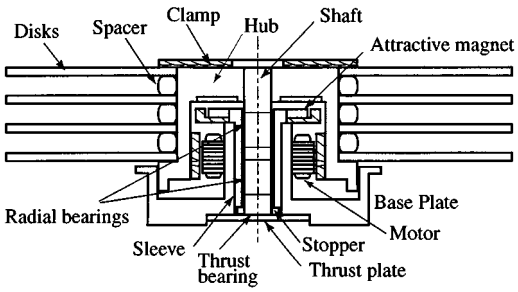

Fig. 2. A rotating-shaft spindle.

II. Mathematical Model

This section outlines the important assumptions, variables, and formulation of the mathematical model. Due to the space limitation, the detail derivation of the model is not presented in this paper. Interested readers should refer to [4], [5] for detail.

Fig. 2 shows a disk-spindle system with rotating-shaft design. The system consists of N elastic circular disks clamped to a deformable hub that allows infinitesimal rigid-body translation and rocking. In addition, the hub is press-fit onto a rotating, flexible shaft, which is mounted to the base through radial and thrust FDB's. Free vibration analysis of rotating-shaft spindles [4] shows that the hub deformation is localized at the hub/shaft interface. To compensate for this localized deformation, the boundary conditions of the flexible shaft at

Manuscript received June 18, 2000. The work of T. Jintanawan was supported by the Mechanical Engineering Department, Chulalongkorn University, Thailand under a Royal Thai Government Scholarship. This work was supported in part by the National Science Foundation under Grant CMS-9820745 and a gift from Electro-Mechanic Advancing Technology Foundation, Japan.

T. Jintanawan is with the Department of Mechanical Engineering, Chulalongkorn University, Bangkok, Thailand 10330 (e-mail: fmetjt@kankrow.eng.chula.ac.th).

I. Y. Shen is with the Department of Mechanical Engineering, University of Washington, Seattle, WA 98195 (e-mail: ishen@u.washington.edu).

K. Tanaka is with NSK Ltd., Fujisawa, Kanagawa, 251-8501, Japan (e-mail: tanaka-kat@nsk.com).

Publisher Item Identifier S 0018-9464(01)02523-7.

the hub/shaft interface (press-fit end) are modeled as a hinged support with a torsional spring. The torsional spring stiffness is determined from the work-energy equation [4]. The fluid bearings are modeled as generalized internal forces through in-line and cross stiffness and damping coefficients. Both radial and thrust bearings are considered. In the present model, the thrust bearings may or may not provide restoring and damping moments against the spindle rocking. Finally, the spindle system is subjected to external forces applied to the disks and base excitations. The base excitations consist of an in-plane and an angular components.

The coupled motion of FDB spindle systems with rotating-shaft design is described by the following degrees-of-freedom: infinitesimal rigid-body translation of the spindle centroid (R_x, R_y, R_z), infinitesimal rigid-body rocking of the hub (θ_x, θ_y), eigenmodes of the flexible shaft ($q_{\hat{x}}$, $q_{\hat{y}}$), and eigenmodes of each disks ($q_{mn}^{(i)}$, $i = 1, 2, \ldots, N$), where the indices m and n refer to disk (m, n) modes with m nodal circles and n nodal diameters.

Equations of motion for FDB spindles with rotating-shaft design are derived through use of Lagrange's equation. Moreover, when all the disks are identical and the spindle system is axisymmetric, the equations of motion can be substantially simplified by using the following complex representation

$$\theta \equiv \theta_x + j\theta_y, \qquad R \equiv R_x + jR_y \tag{1}$$

$$Q_{mn}^{(i)} \equiv q_{m,-n}^{(i)} - jq_{mn}^{(i)}, \qquad q \equiv q_{\hat{x}} + jq_{\hat{y}} \tag{2}$$

where $j \equiv \sqrt{-1}$. Because of the insignificance of the disk vibration modes with one or more nodal circles, only the zero-nodal-circle modes are retained in the equations of motion. As a result, the equations of motion can be separated into three sets of coupled equations: a) coupled hub translation-rocking, shaft deflection, and (0, 1) disk modes, b) coupled axial hub translation and (0, 0) disk modes, and c) disk modes with two or more nodal diameters. The first set of equations a) is the most critical for HDD, because the motion has a significant in-plane component causing track misregistration. Therefore, this paper will only focus on the first set of equations of motion.

The matrix equation of motion governing the hub rocking and (0, 1) modes is

$$\mathbf{M}_1\ddot{\mathbf{q}}_1(t) + \mathbf{C}_1\dot{\mathbf{q}}_1(t) + \mathbf{K}_1\mathbf{q}_1(t) = \mathbf{f}_1(t) + \mathbf{h}_1(t) \tag{3}$$

where

- $\mathbf{q}_1$ is the vector of generalized coordinates,
- $\mathbf{M}_1$ is the inertia matrix,
- $\mathbf{C}_1$ is the complex gyroscopic and damping matrix, and
- $\mathbf{K}_1$ is the complex stiffness and oscillatory matrix given by

$$\mathbf{q}_1 = \left(\theta, R, q, Q_{01}^{(1)}, Q_{01}^{(2)}, \ldots, Q_{01}^{(N)}\right)^T \tag{4}$$

$$\mathbf{M}_1 = \begin{bmatrix} \eta_1 & 0 & j\alpha_1 & a_0 & a_0 & \ldots & a_0 \\ 0 & \eta_0 & \lambda_1 & 0 & 0 & \ldots & 0 \\ -j\alpha_1 & \lambda_1 & \eta_2 & 0 & 0 & \ldots & 0 \\ a_0 & 0 & 0 & 1 & 0 & \ldots & 0 \\ a_0 & 0 & 0 & 0 & 1 & \ldots & 0 \\ \vdots & \vdots & \vdots & \vdots & \vdots & \ddots & \vdots \\ a_0 & 0 & 0 & 0 & 0 & \ldots & 1 \end{bmatrix} \tag{5}$$

$$\mathbf{C}_1 = \begin{bmatrix} c_{\theta\theta} & c_{\theta R} & c_{\theta q} & \psi & \psi & \ldots & \psi \\ -c_{\theta R} & c_{RR} & c_{Rq} & 0 & 0 & \ldots & 0 \\ -c_{\theta q} & c_{Rq} & c_{qq} & 0 & 0 & \ldots & 0 \\ \psi & 0 & 0 & c_{01} & 0 & \ldots & 0 \\ \psi & 0 & 0 & 0 & c_{01} & \ldots & 0 \\ \vdots & \vdots & \vdots & \vdots & \vdots & \ddots & \vdots \\ \psi & 0 & 0 & 0 & 0 & \ldots & c_{01} \end{bmatrix} \tag{6}$$

$$\mathbf{K}_1 = \begin{bmatrix} k_{\theta\theta} & k_{\theta R} & k_{\theta q} & 0 & 0 & \ldots & 0 \\ -k_{\theta R} & k_{RR} & k_{Rq} & 0 & 0 & \ldots & 0 \\ -k_{\theta q} & k_{Rq} & k_{qq} & 0 & 0 & \ldots & 0 \\ 0 & 0 & 0 & k_{01} & 0 & \ldots & 0 \\ 0 & 0 & 0 & 0 & k_{01} & \ldots & 0 \\ \vdots & \vdots & \vdots & \vdots & \vdots & \ddots & \vdots \\ 0 & 0 & 0 & 0 & 0 & \ldots & k_{01} \end{bmatrix}. \tag{7}$$

Also, $\mathbf{f}_1(t)$ and $\mathbf{h}_1(t)$ are vectors of generalized forces associated with the external loads and base excitations, respectively, given by

$$\mathbf{f}_1(t) = \frac{1}{I_1}\begin{pmatrix} j\sum_{i=1}^{N}\int \left\{z_i\left[g_x^{(i)} + jg_y^{(i)}\right] - \mathrm{r}_0 g_z^{(i)}\right\} dA_0^{(i)} \\ \sum_{i=1}^{N}\int \left[g_x^{(i)} + jg_y^{(i)}\right] dA_0^{(i)} \\ 0 \\ \int g_z^{(1)}[w_{0,-1} - jw_{01}]\, dA_0^{(1)} \\ \vdots \\ \int g_z^{(N)}[w_{0,-1} - jw_{01}]\, dA_0^{(N)} \end{pmatrix} \tag{8}$$

$$\mathbf{h}_1(t) = \frac{1}{I_1}\begin{pmatrix} c_\theta\dot{\gamma} + k_\theta\gamma \\ -M\ddot{s} + c_R\dot{\gamma} + k_R\gamma \\ -M_{s1}\ddot{s} + c_q\dot{\gamma} + k_q\gamma \\ 0 \\ \vdots \\ 0 \end{pmatrix}. \tag{9}$$

Description of each term in $\mathbf{M}_1$, $\mathbf{C}_1$, $\mathbf{K}_1$, $\mathbf{f}_1$, and $\mathbf{h}_1$ is explained in Appendix with great detail.

Solution of (3) is obtained through Laplace transforms and convolution integral; see [2] and [5] for detail. Specifically, transfer matrices from Laplace transforms and Green's functions from convolution integral determine FRF's and time responses, respectively.

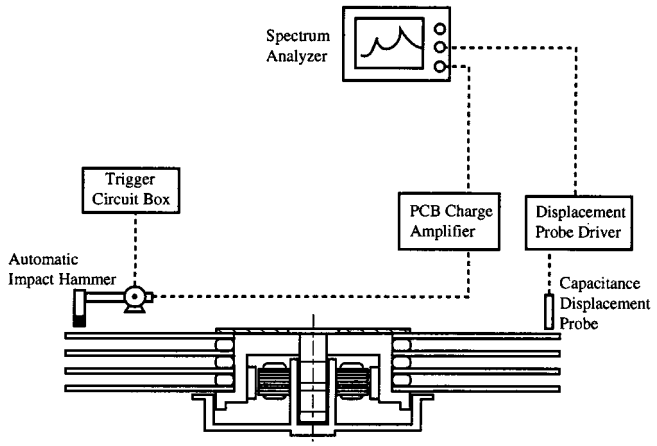

Fig. 3. Experimental setup.

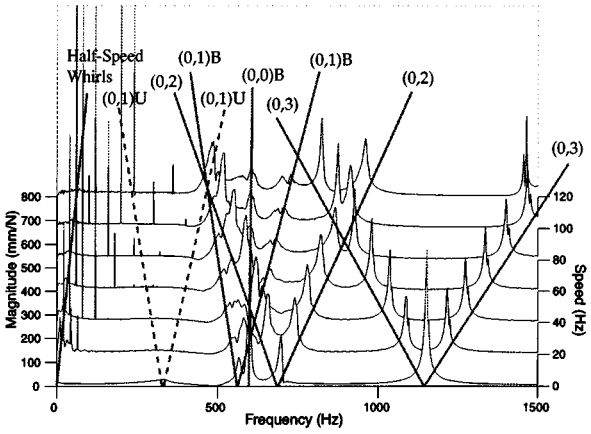

Fig. 4. Experimental waterfall plot of a FDB spindle with rotating shaft; 4-disk spindle.

TABLE I
GEOMETRY AND PROPERTIES OF THE FDB SPINDLE

Disk		Bearings	
b	47.50 mm	$k_{1a}^{(r)}$	17.272 x ω_3 N/mm
a	16.50 mm	$k_{2a}^{(r)}$	21.857 x ω_3 N/mm
I_1	8.561 kg-mm^2	$k_{1b}^{(r)}$	19.417 x ω_3 N/mm
I_3	17.12 kg-mm^2	$k_{2b}^{(r)}$	27.233 x ω_3 N/mm
m	1.346 x 10^{-2} kg	z_a	- 5.876 mm
z_1	- 4.226 mm	z_b	-2.226 mm
z_2	- 1.426 mm	$c_{1a}^{(r)}$	4.158 x 10^4 Ns/m
z_3	1.375 mm	$c_{1b}^{(r)}$	5.188 x 10^4 Ns/m
z_4	4.175 mm	Shaft	
		l_s	10.5 mm
Hub		d_s	4.2 mm
I_1	2.177 kg-mm^2	$\hat{z}_a$	3.55 mm
I_3	3.693 kg-mm^2	$\hat{z}_b$	7.20 mm
m	2.488 x 10^{-2} kg	E_s	210 GPa
		ρ_s	7800 kg/m^3

III. EXPERIMENTAL SETUP

Fig. 3 shows the experimental setup. In the experiment, the spindle spins at a constant speed. An automatic impact hammer [6] applies an impact force to the outer rim of the top disk in the transverse direction. In addition, a capacitance probe measures the transverse vibration of the top disk. Both the force and vibration signals are sent to a spectrum analyzer to calculate FRF's. The experiment is then repeated at other speeds.

The FDB spindle used in the experiments was sponsored by NSK Ltd., Japan. The spindle carries four identical disks with thickness of 0.8 mm. In addition, the spindle is supported by two radial bearings and a thrust bearing. The geometry and properties of this spindle are listed in Table I. For the disk section of Table I, a and b are inner and outer radius of the disk, I_1 and I_3 are the transverse and polar mass moment of inertia about the disk center, z_1, z_2, z_3 and z_4 are location of the disks with respect to the centroid of the disk pack, and m is the mass of the disk. For the bearing section of Table I, the subscripts a and b refer to the lower and upper bearings, the subscripts 1 and 2 refer to the in-line and cross bearing coefficients, and the superscript (r) refers to radial bearings. The variables k, c, and z represent stiffness, damping, and location of the bearings with respect to the disk pack centroid. Note that stiffness coefficients $k_{1a}^{(r)}$, $k_{2a}^{(r)}$, $k_{1b}^{(r)}$, and $k_{2b}^{(r)}$ of the radial bearings in Table I are proportional to the rotational speed ω_3, where ω_3 is in rad/s. The bearing coefficients were calculated through *MTI CARDENCE Program CAD-42I*, and were also verified by other calculation methods. Also note that the thrust bearing coefficients are not listed in Table I because of the space limitation. Basically, the spindle is supported axially by a single thrust bearing with an attractive magnet; see Fig. 2. Therefore, the bearing clearance is not a constant and highly depends on the spin speed. As a result, simple formula like $k_{1a}^{(r)}$ in Table I for radial bearings cannot be obtained. In general, the stiffness and damping coefficients of the thrust bearing decrease as the spin speed increases. Finally, for the shaft section of Table I, parameters l, d, E, and ρ represent the length, diameter, Young's modulus, and density of the shaft. Also, $\hat{z}_a$ and $\hat{z}_b$ are the location of the bearings measured from the bottom (not the fixed end) of the shaft.

IV. EXPERIMENTAL RESULTS

Fig. 4 shows the waterfall plot of the FDB spindle from 0 to 7200 rpm. The transverse load applied to the disk excites two types of modes: disk modes and spindle modes. Disk modes include (0, 0)B, (0, 1) B, (0, 2) and (0, 3) modes. Spindle modes include half-speed whirls and unbalanced (0, 1) modes [denoted by (0, 1)U], which is also known as rocking modes in HDD industry. For disk modes, only the disks experience deformation resulting in axial displacement only. In contrast, spindle modes have both bearing and disk deformation resulting both axial and radial displacement components.

Inspection of Fig. 4 shows that the amplitude of the rocking modes is substantially reduced from 30 μm/N to 20 μm/N when the FDB spindle spins up. Also, splitting of the rocking modes into backward and forward components is not observed in Fig. 4. This probably results from increased flexibility as the system spins up. When the spindle is stationary, the spindle rests on the thrust bearing through metal-to-metal contact, which serves as a fixed-end boundary condition. When the spindle spins up, the spindle floats on the thrust bearing surface through a lubrication film, which serves as a viscoelastic foundation. The transition of the thrust bearing boundary condition from a fixed end to a viscoelastic foundation increases the flexibility and consequently the damping of the system. Note that the increased

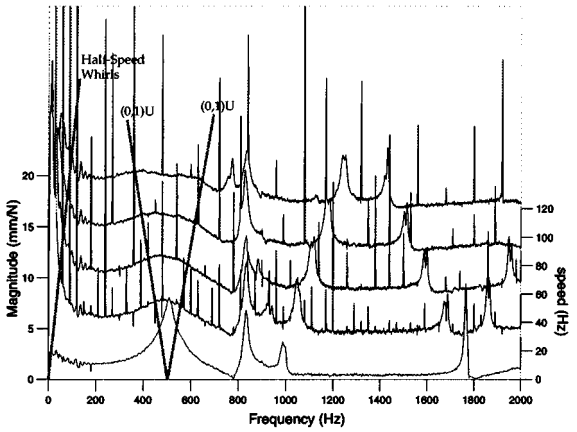

Fig. 5. Experimental waterfall plot of a FDB spindle with rotating shaft; 1-disk spindle.

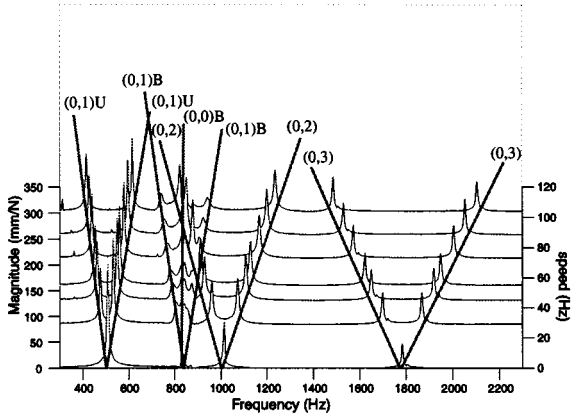

Fig. 6. Experimental waterfall plot of a ball-bearing spindle with rotating shaft.

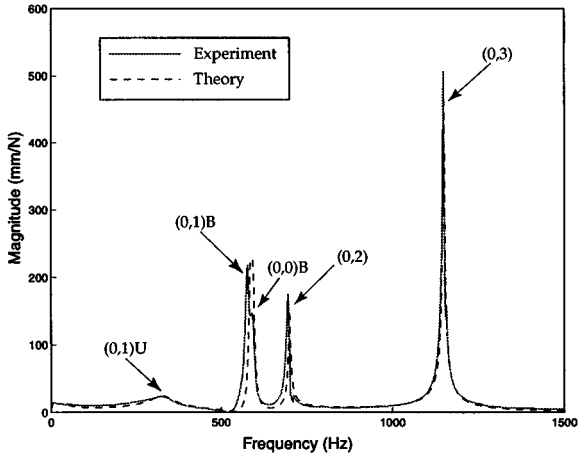

Fig. 7. Experimental and theoretical FRF's of the FDB spindle; $\omega_3 = 0$ Hz.

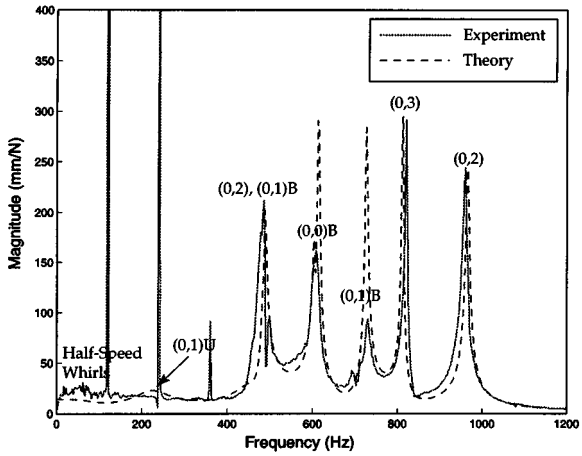

Fig. 8. Experimental and theoretical FRF's of the FDB spindle; $\omega_3 = 120$ Hz.

flexibility does not significantly reduce the natural frequencies of the rocking modes. This can be observed when the spindle carries only one disk; see the waterfall plot shown in Fig. 5. Fig. 5 shows shallow resonance peaks for backward and forward rocking modes when $\omega_3 = 120$ Hz. Clearly, the frequency splits around that of the stationary spindle.

To investigate the effect of FDB's, experimental waterfall plots of a FDB spindle (Fig. 4) and a ball-bearing spindle (Fig. 6) with rotating-shaft design are qualitatively compared. Comparison of Figs. 4 and 6 shows that FDB's damp out the rocking modes (0, 1)U, which are the critical vibration modes for HDD. Moreover, FDB's induce the half-speed whirls with small amplitude. Note that the disk modes of the ball-bearing spindle have smaller amplitude. This is because the ball-bearing spindles carries two disks with 1.27-mm thickness (versus 0.8-mm disk thickness in FDB spindles).

V. Experimental Verification

Theoretical predictions of FRF's are compared with experimental measurements to validate the mathematical model. Figs. 7 and 8 show the comparison at $\omega_3 = 0$ and 120 Hz, respectively. First of all, (0, 2) and (0, 3) disk modes from the theoretical predictions match well with the experimental results in both natural frequencies and resonance amplitudes. In addition, the natural frequencies of (0, 1)B and (0, 0)B modes from the predictions agree well with the experimental frequencies. The theoretical and experimental resonance amplitudes of the balanced modes at $\omega_3 = 0$ also agree very well. When $\omega_3 \neq 0$, these resonance amplitudes cannot be compared because there exists broken peaks of the balanced modes in the measurement. These broken peaks may result from the unbalanced disks or the imperfection of the disks.

Fig. 9 shows theoretical and experimental FRF's of the same spindle at $\omega_3 = 0,\ 30,\ 60$, and 90 Hz, focusing on the half-speed whirls and rocking modes. The theoretical and experimental results in Fig. 9 match well in both shape and resonance frequencies. For resonance amplitudes, however, there is a discrepancy between the theoretical and experimental results.

There are probably several factors contributing to the discrepancy. The first factor is the uncertainties of the bearing coefficients listed in Table I. Because the exact temperature of the lubricant inside the bearings is unknown, the viscosity of the lubricant can only be estimated. This results in some uncertainties in the calculated radial bearing stiffness and damping coefficients.

The second factor is the bearing width. The theoretical model assumes that the bearing stiffness and damping are lumped at the

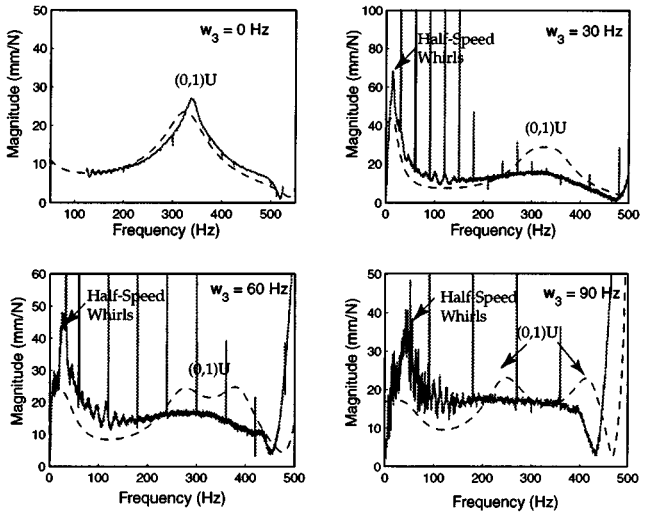

Fig. 9. Half-speed whirls and unbalanced (0, 1) modes; solid line for theory, and dash line for experiment.

center of each bearing. In reality, the width of the fluid bearings is not infinitesimal. How much the bearing width affects the spindle response remains open thus far.

The third factor might be the thrust bearing coefficients. The theoretical calculations in Fig. 9 assume that the thrust bearing has constant bearing coefficients. Under this assumption, the damping of (0, 1) unbalanced modes remains unchanged, because the damping of the radial bearings is almost independent of the spin speeds. Consequently, the theoretical results in Fig. 9 predict an amplitude around 30 μm/N for the (0, 1) unbalanced modes, when the spin speed varies from 30 to 90 Hz. The experimental data, however, indicate an increase in damping for (0, 1) unbalanced modes as the spin speed increases. This might result from the thrust bearing coefficients, because they vary significantly with respect to the spin speed.

VI. Conclusions

1) Fundamental vibration characteristics, such as balanced and unbalanced modes, remain valid for spindles with rotating-shaft design.
2) FDB spindles significantly damp out the rocking modes, but induce small half-speed whirls.
3) A preliminary numerical simulation, based on the mathematical model, predicts FRF's of rotating-shaft FDB spindles with reasonable accuracy. The model captures major characteristics of FDB spindles, such as half-speed whirls and (0, 1) unbalanced modes. Nevertheless, fine tuning of the mathematical model is needed to further improve the accuracy of the model.

Appendix

In (5) and (6)

$$\eta_0 \equiv \frac{M}{I_1} \qquad \eta_1 \equiv \frac{\overline{I}_1}{I_1} \qquad \eta_2 \equiv \frac{\hat{I}_s}{I_1} \qquad \eta_3 \equiv \frac{\overline{I}_3}{I_1} \tag{10}$$

$$\lambda_1 \equiv \frac{M_{s1}}{I_1} \qquad \lambda_2 \equiv \frac{M_{s2}}{I_1} \qquad \alpha_1 \equiv \frac{N_{s1}}{I_1} \qquad \alpha_2 \equiv \frac{N_{s2}}{I_1} \tag{11}$$

and

$$a_0 = \frac{\pi\rho h}{I_1} \int_a^b R_{m1}(r) r^2 \, dr \tag{12}$$

where

M is the total mass of the disk-spindle system,
$\overline{I}_1$ and $\overline{I}_3$ are the centroidal mass moment of inertia of the disk-spindle system about the x and y axes, and
I_1 is the diametral mass moment of inertia of each disk.

In addition, M_{s1}, M_{s2}, N_{s1}, N_{s2}, and $\hat{I}_s$ are the modal masses of the shaft defined in [5].

In (6)

$$c_{\theta\theta} = -j\omega_3\eta_3 + \frac{1}{I_1}\left[\sum_r z_b^2 C^{(r)} + \sum_t C^{(t)}\right] \tag{13}$$

$$c_{\theta R} = \frac{j}{I_1}\sum_r \left[z_b C^{(r)}\right] \qquad c_{RR} = \frac{1}{I_1}\sum_r C^{(r)} \tag{14}$$

$$c_{\theta q} = \omega_3\alpha_2 + \frac{j}{I_1}\left[\sum_r z_b\phi(\hat{z}_b)C^{(r)} + \sum_t \frac{\partial\phi(\hat{z}_b)}{\partial\hat{z}} C^{(t)}\right] \tag{15}$$

$$c_{Rq} = \frac{1}{I_1}\sum_r \left[\phi(\hat{z}_b)C^{(r)}\right] \tag{16}$$

$$c_{qq} = +\frac{1}{I_1}\left\{\sum_r \left[\phi^2(\hat{z}_b)C^{(r)}\right] + \sum_t \left[\frac{\partial\phi(\hat{z}_b)}{\partial\hat{z}}\right]^2 C^{(t)}\right\} - j\omega_3\lambda_2 + \frac{c_s}{\rho_s A_s} \tag{17}$$

$$\psi = -2j\omega_3 a_0 \tag{18}$$

and

$$c_{01} = \zeta - 2j\omega_3 \tag{19}$$

where

z_b and $\hat{z}_b$ are the position of the bearings measured with respect to the system centroid and the lower end of the shaft, respectively,
$\phi(\hat{z}_b)$ is the 1st mode shape of the shaft, and
$\sum_r$ and $\sum_t$ mean summation over all the radial and thrust FDB's, respectively.

In addition, $C^{(r)}$ and $C^{(t)}$ are complex damping constants defined as

$$C^{(r)} = c_1^{(r)} - jc_2^{(r)} \qquad C^{(t)} = c_1^{(t)} - jc_2^{(t)}. \tag{20}$$

Note that $c_1^{(\alpha)}$ and $c_2^{(\alpha)}$ ($\alpha = r, t$) are the in-line and off-diagonal damping coefficients of the bearings, respectively. Also c_s is the shaft viscous damping coefficient, ρ_s is the shaft density, A_s is the shaft cross section area, and ζ is the normalized viscous damping of the disks defined in [5].

Similarly, if $K^{(r)}$ and $K^{(t)}$ are complex stiffness coefficients defined as

$$K^{(r)} = k_1^{(r)} - jk_2^{(r)} \qquad K^{(t)} = k_1^{(t)} - jk_2^{(t)} \tag{21}$$

then in (7)

$$k_{\theta\theta} = \frac{1}{I_1}\left[\sum_r z_b^2 K^{(r)} + \sum_t K^{(t)}\right] \tag{22}$$

$$k_{\theta q} = \frac{j}{I_1}\left[\sum_r z_b\phi(\hat{z}_b)K^{(r)} + \sum_t \frac{\partial\phi(\hat{z}_b)}{\partial\hat{z}} K^{(t)}\right] \tag{23}$$

$$k_{qq} = \omega_s^2 + \frac{1}{I_1}\left\{\sum_r \left[\phi^2(\hat{z}_b)K^{(r)}\right] + \sum_t \left[\frac{\partial\phi(\hat{z}_b)}{\partial\hat{z}}\right]^2 K^{(t)}\right\} \tag{24}$$

and

$$k_{01} = \omega_{01}^2 - \omega_3^2 - j\zeta\omega_3 \tag{25}$$

where ω_{01} is the natural frequencies of the disks. In addition, coefficients $k_{\theta R}$, k_{RR}, and k_{Rq} in (7) can be found from (14) and (16) with all c replaced by k.

In (8) and (9), z_i is the position of the ith disk measured with respect to the system centroid, $\mathbf{r}_0$ is the point of applied load, $g_x^{(i)}$, $g_y^{(i)}$, and $g_z^{(i)}$ are the external load applied to the ith disk in x, y, and z directions, and $w_{0n}(n = 1, -1)$ are the mode shapes of the disks. Also

$$\begin{aligned} c_\theta &= \sum_r z_b\hat{z}_b C^{(r)} + \sum_t C^{(t)} \\ c_R &= -j\sum_r \left[\hat{z}_b C^{(r)}\right], \\ c_q &= -j\left[\sum_r \hat{z}_b\phi(\hat{z}_b)C^{(r)} + \sum_t \frac{\partial\phi(\hat{z}_b)}{\partial\hat{z}}\, C^{(t)}\right] \end{aligned} \tag{26}$$

k_θ, k_R, k_q can be determined from (26) by replacing all c with k. Moreover, s is the in-plane base excitation and γ is the angular base excitation defined as

$$s = s_x + js_y \qquad \gamma = \gamma_x + j\gamma_y. \tag{27}$$

REFERENCES

[1] I. Y. Shen and C.-P. Roger Ku, "A nonclassical vibration analysis of multiple rotating disk/spindle system," *ASME J. Appl. Mech.*, vol. 64, pp. 165–174, 1997.

[2] I. Y. Shen, "Closed-form forced response of a damped, rotating, multiple disk/spindle system," *ASME J. Appl. Mech.*, vol. 64, pp. 343–352, 1997.

[3] T. Jintanawan, I. Y. Shen, and C.-P. Roger Ku, "Free and forced vibration of a rotating disk pack and spindle motor system with hydrodynamic bearings," *J. Inf. Storage and Process. Syst.*, vol. 1, pp. 45–58, 1999.

[4] T. Jintanawan and I. Y. Shen, "Free vibration of a rotating disk pack and spindle motor system with rotating-shaft design," *J. Inf. Storage and Process. Syst.*, vol. 2, pp. 129–139.

[5] T. Jintanawan, "Vibration of rotating disk-spindle systems with hydrodynamic bearings," Ph.D. dissertation, University of Washington, 2000.

[6] H. Bittner and I. Y. Shen, "Taming disk/spindle vibrations through aerodynamic bearings and acoustically tuned-mass dampers," *IEEE Trans. Magn.*, vol. 35, pp. 827–832, 1999.